Research Square

Preprints are preliminary reports that have not undergone peer review.
They should not be considered conclusive, used to inform clinical practice,
or referenced by the media as validated information.

Symmetry-engineered and electrically tunable in-plane anomalous Hall effect in oxide heterostructures

Lingfei Wang

wanglf@ustc.edu.cn

University of Science and Technology of China https://orcid.org/0000-0003-1675-0941

Kunjie Dai

University of Science and Technology of China

Zhen Wang

University of Science and Technology of China https://orcid.org/0000-0003-3613-3238

Wenfeng Wu

Institute of Solid State Physics, HFIPS, Chinese Academy of Sciences

Feng Jin

University of Science and Technology of China https://orcid.org/0000-0002-5688-0364

Enda Hua

University of Science and Technology of China

Nan Liu

Northwest University

Jingdi Lu

Hefei National Research Center for Physical Sciences at Microscale, University of Science and Technology of China

Jinfeng Zhang

University of Science and Technology of China

Yuyue Zhao

University of Science and Technology of China

Linda Yang

University of Science and Technology of China

Kai Liu

University of Science and Technology of China

Huan Ye

University of Science and Technology of China

Qiming Lv

University of Science and Technology of China

Zhengguo Liang
University of Science and Technology of China
Ao Wang
University of Science and Technology of China
Dazhi Hou
University of Science and Technology of China https://orcid.org/0000-0002-1286-2965
Yang Gao
University of Science and Technology of China https://orcid.org/0000-0002-9223-0633
Jing Tao
University of Science and Technology of China
Liang Si
Northwest University https://orcid.org/0000-0003-4709-6882
Wenbin Wu Wu
University of Science and Technology of China

Article

Keywords:

Posted Date: April 8th, 2026

DOI: https://doi.org/10.21203/rs.3.rs-9297012/v1

License: This work is licensed under a Creative Commons Attribution 4.0 International License.
Read Full License

Additional Declarations: There is **NO** Competing Interest.

Version of Record: A version of this preprint was published at Nature Communications on October 6th, 2026. See the published version at https://doi.org/10.1038/s41467-026-78350-x.

Symmetry-engineered and electrically tunable in-plane anomalous Hall effect in oxide heterostructures

Kunjie Dai[1,6], Zhen Wang[2,6], Wenfeng Wu[3,4,6], Feng Jin[1], Enda Hua[1], Nan Liu[4], Jingdi Lu[1], Jinfeng Zhang[1], Yuyue Zhao[1], Linda Yang[1], Kai Liu[1], Huan Ye[1], Qiming Lv[1], Zhengguo Liang[1], Ao Wang[1], Dazhi Hou[1,2], Yang Gao[2], Jing Tao[2], Liang Si[4]*, Wenbin Wu[1,5]*, and Lingfei Wang[1]*

[1] Hefei National Research Center for Physical Sciences at the Microscale, University of Science and Technology of China, Hefei 230026, China.

[2] Department of Physics, University of Science and Technology of China, Hefei 230026, China.

[3] Key Laboratory of Materials Physics, Institute of Solid State Physics, HFIPS, Chinese Academy of Sciences, Hefei 230031, China.

[4] School of Physics, Northwest University, Xi'an 710127, China.

[5] Anhui Key Laboratory of Condensed Matter Physics at Extreme Conditions, High Magnetic Field Laboratory, Chinese Academy of Sciences, Hefei 230031, China.

[6] These authors contribute equally to this work: Kunjie Dai, Zhen Wang, Wenfeng Wu.

* Corresponding author. Email: wanglf@ustc.edu.cn, wuwb@ustc.edu.cn, siliang@nwu.edu.cn.

Abstract

Anomalous Hall effect (AHE) has long served as a cornerstone for uncovering low-dissipation quantum phenomena and powering Hall-based functionalities, yet its tunability and device application are both constrained by the orthogonal relationship among electric field, Hall current, and out-of-plane magnetization in thin film geometry. The recently emerged in-plane anomalous Hall effect (IP-AHE), a transverse Hall response driven by in-plane magnetization, promises to unlock Hall readout of planar magnetic orders and spin textures. However, in sharp contrast to conventional AHE, experimentally accessible and effective control strategies for IP-AHE remain largely undeveloped, impeding its transition from phenomenological observation to device implementation. Here we establish a symmetry-engineered, electrically tunable IP-AHE in epitaxial $CaRuO_3/La_{2/3}Ca_{1/3}MnO_3/CaRuO_3$ heterostructures grown on $NdGaO_3(110)$. By exploiting $CaRuO_3$-buffer-controlled mirror-symmetry breaking in the ferromagnetic $La_{2/3}Ca_{1/3}MnO_3$ layer, we achieve a robust IP-AHE that faithfully mirrors square-shaped ferromagnetic hysteresis, providing a direct Hall readout of in-plane magnetization reversal. Ionic liquid gating further enables dynamic reconfiguration of the symmetry breaking, achieving wide-range electrical modulation and fully reversible ON/OFF switching of IP-AHE. This highly tunable IP-AHE platform offers a symmetry-based probe of emergent low-dimensional magnetism and facilitates the development of programmable Hall functionalities in planar device geometries.

Anomalous Hall effect (AHE) has played a central role over the past century in revealing intriguing magnetic/topological orders in condensed matter and enabling a wide range of spintronic functionalities[1-3]. In the conventional AHE geometry, the three vectors, magnetization (***M***), longitudinal electric field (***E***), and transverse Hall current density ($\boldsymbol{j}_{\mathrm{AHE}}$), are mutually orthogonal (Fig. 1a). In magnetic thin films and layered magnets, this orthogonal geometry makes the AHE signal sensitive to the out-of-plane ***M*** component but insensitive to the in-plane component[4-6]. In practical spintronic devices, this constraint restricts Hall readout of magnetic switching in out-of-plane geometry only[3]. Nevertheless, the Onsager relationship does not mandate such orthogonal constraint for AHE[7]. Recent theoretical calculations also suggest that simultaneously breaking the time-reversal-symmetry and mirror-symmetry may allow an in-plane ***M*** to generate a transverse Hall response, giving rise to the so-called in-plane AHE (IP-AHE, Fig. 1b)[8-13]. Subsequent magnetotransport experiments on layered magnets have corroborated this scenario[14-18]. For example, in the V_2S-VS superlattice with *C*2/*m* symmetry, IP-AHE emerges when an in-plane $\boldsymbol{M}\perp[010]$ breaks the remaining mirror-symmetry[14]. In the ferromagnetic semimetal Fe_3Sn_2 and $Co_3Sn_2S_2$ with $R\bar{3}m$ symmetry, IP-AHE arises from the in-plane $\boldsymbol{M}\perp[100]$ axis, which eliminates the three-fold perpendicular mirror planes[16,17]. These advances established the central role of mirror-symmetry breaking in activating IP-AHE. However, due to the strict symmetry requirements, experimental observations of IP-AHE have so far been limited to weakly magnetized two-dimensional materials[14,15], Kagome magnets[16], and magnetic Weyl semimetals[17,18], most of which exhibit weak in-plane magnetic anisotropy (MA). Such a limited materials landscape has so far hindered the establishment of a definitive, one-to-one correspondence among mirror-symmetry breaking, IP-AHE, and in-plane ferromagnetism. Consequently, experimentally accessible strategy for effective control of IP-AHE remain largely undeveloped, posing a major obstacle to its device implementation.

In contrast to the aforementioned layered magnets with nearly invariant structural symmetry, ABO_3 perovskite oxide heterostructures offer extensive tunability in both lattice symmetry and magnetism. The lattice symmetries of perovskite oxides are intimately tied to the deformation and collective rotation patterns of the BO_6 oxygen octahedra framework[19,20]. Specific oxygen octahedral rotation (OOR) patterns (in Glazer notation), such as $a^0a^0a^0$, $a^-a^-a^-$, and $a^-a^-c^+$, lead to cubic, rhombohedral, and orthorhombic symmetries, respectively[21,22]. By stacking the perovskite oxides into epitaxial heterostructures, their OOR patterns and corresponding lattice symmetry can

be flexibly engineered through various factors, such as epitaxial strain, interface structure, proton-intercalation, and chemical doping[19]. Meanwhile, the intricate interplay between spin-orbit coupling (SOC) and electron-electron correlations in these heterostructures gives rise to a rich array of magnetic orders, along with highly tunable MA and AHE[3-5, 23-26]. Furthermore, the strong coupling between the spin, lattice, orbital, and charge degrees of freedom ensures tight links among the structural symmetry, magnetic order, and AHE[27-29]. Collectively, these attributes make perovskite oxide heterostructures an ideal platform for achieving highly tunable IP-AHE.

In this study, we exploit the structural tunability of perovskite oxides to design a symmetry-engineered, electrically-tunable IP-AHE platform: a $CaRuO_3/La_{2/3}Ca_{1/3}MnO_3/CaRuO_3$ (CRO/LCMO/CRO) epitaxial heterostructure, which converts stringent mirror-symmetry breaking constraints into deterministic and effective tuning knobs for IP-AHE. In this ferromagnetic trilayer heterostructure, $CaRuO_3$ buffer-controlled mirror-symmetry breaking and uniaxial in-plane magnetic anisotropy cooperatively activate a highly tunable IP-AHE that faithfully reproduces the square-shaped ferromagnetic hysteresis. Ionic liquid gating further introduces reversible protonation in the $CaRuO_3$ buffer to reconfigure the symmetry-breaking *in situ*, enabling wide-range electrical modulation and ON/OFF switching of IP-AHE (Fig. 1b). This symmetry-tailored, electrically controllable IP-AHE platform can serve as a sensitive probe of nontrivial in-plane spin textures/magnetic orders and open pathways towards programmable Hall functionalities in spintronic devices with planar geometries.

Observation of IP-AHE in CRO/LCMO/CRO/NGO(110)$_O$ trilayers

We deposit a series of CRO/LCMO/CRO trilayer heterostructures on the $(110)_O$-oriented $NdGaO_3$ [NGO$(110)_O$, where the subscript "O" denotes orthorhombic indices] substrates by pulsed laser deposition. The perovskite-structured LCMO, CRO, and NGO share the same orthorhombic *Pbnm* (No. 62) symmetry, arising from the collective in-plane and out-of-plane OOR ($a^-a^-c^+$ in Glazer notation, Fig. 1c)[19,22]. Reflection high-energy electron diffraction monitoring confirms that both the CRO and LCMO layers grow in a standard layer-by-layer mode (Supplementary Fig. 1), enabling a unit-cell-level control of the CRO and LCMO layer thicknesses [denoted as t_{CRO} and t_{LC}, in unit-cells (u.c.)]. X-ray diffraction (XRD) 2θ-ω linear scans and atomic force microscopy confirm the high epitaxial quality of CRO/LCMO/CRO trilayer heterostructures (Supplementary Fig. 2). XRD reciprocal space mappings (RSMs) further demonstrate that these heterostructures are coherently strained to the NGO$(110)_O$ substrates (Supplementary Fig. 3).

Consistent with the excellent epitaxial quality and structural coherency, the CRO/LCMO/CRO/NGO(110)$_O$ trilayer heterostructure displays strong ferromagnetism with an in-plane uniaxial MA. The temperature-dependent M (M-T) and longitudinal resistivity (ρ_{xx}-T) curves of the trilayers reveal clear paramagnetic-insulator to ferromagnetic-metal (FMM) transitions upon cooling (Supplementary Fig. 4). The high Curie temperature ($T_C \geq 250$ K) indicates that the FMM state originates predominantly from the LCMO layer rather than the CRO layer or the CRO/LCMO interface. The increases in T_C and saturated M (M_s) with t_{CRO} suggest that the CRO layers stabilize the FMM phase in LCMO layers, likely through interfacial charge transfer from Ru^{4+} to Mn^{4+} cations[30-32]. As depicted in Fig. 1d-f, we measure the magnetic field-dependent M (M-H) curves of a representative CRO(16 u.c.)/LCMO(32 u.c.)/CRO(16 u.c.)/NGO(110)$_O$ at 10 K, with $\boldsymbol{H}$ applied along the [001]$_O$ axis, [$\bar{1}$10]$_O$ axis, and the film normal [$\perp$(110)$_O$ plane]. The out-of-plane M-H curves [$\boldsymbol{H}\perp$(110)$_O$ plane] display negligible M (Fig. 1d), and the in-plane curve measured with $\boldsymbol{H}$//[001]$_O$ displays a slanted hysteresis loop (Fig. 1e), where M saturates at a saturation field $H_S \approx 2000$ Oe. In sharp contrast, $\boldsymbol{H}$//[$\bar{1}$10]$_O$ yields a square-shaped ferromagnetic hysteresis loop with a small coercive field $H_C \sim 200$ Oe (Fig. 1f), establishing the in-plane magnetic easy-axis along LCMO[$\bar{1}$10]$_O$. Since LCMO intrinsically has weak SOC and negligible magnetocrystalline anisotropy, the in-plane uniaxial MA is governed primarily by demagnetization energy and magnetoelastic contributions arising from NGO(110)$_O$-imposed anisotropic strain[33]. Additionally, the CRO layers, which possess stronger SOC, likely amplify this magnetoelastic coupling and thereby reinforce a robust in-plane uniaxial MA[5,34].

Together with the in-plane uniaxial MA, the CRO/LCMO/CRO/NGO(110)$_O$ trilayers exhibit unique Hall transport. Consistent with the M-H measurements, we apply $\boldsymbol{H}$ along the three orthogonal axes, set $\boldsymbol{E}$//[$\bar{1}$10]$_O$ axis, and measure the transverse Hall resistivity (ρ_{xy}) along the [001]$_O$ axis (Fig. 1d-f). We subtract the linear component of the ρ_{xy}-H curves by fitting the $H > H_S$ regimes and obtain the H-dependent anomalous Hall resistivity (ρ_{AHE}-H) curves. In the conventional Hall geometry [$\boldsymbol{H}\perp$(110)$_O$], the ρ_{AHE} signal is negligible (Fig. 1d), consistent with the in-plane MA revealed by the M-H curves. When $\boldsymbol{H}$//[$\bar{1}$10]$_O$ (the in-plane easy axis), the ρ_{AHE}-H curve surprisingly shows an inverted ferromagnetic hysteresis loop (Fig. 1f), which closely tracks the line shape of the corresponding M-H hysteresis loop. The ρ_{AHE} signal, proportional to the in-plane $\boldsymbol{M}$ along [$\bar{1}$10]$_O$, strongly suggests the emergence of IP-AHE. By contrast, when $\boldsymbol{H}$//[001]$_O$ (in-plane magnetic hard axis), the ρ_{AHE}-H curve (Fig. 1e) displays an unusual hysteresis

loop: ρ_{AHE} remains finite at $H = 0$, close to the value for the $\boldsymbol{H}//[\bar{1}10]_O$ case. Upon increasing H, ρ_{AHE} gradually decreases and eventually vanishes near $H_S \approx 2000$ Oe. When $H < H_S$, the in-plane uniaxial MA keeps a sizable $\boldsymbol{M}$ component aligned with the easy axis $[\bar{1}10]_O$ (Fig. 1f), thereby sustaining a finite ρ_{AHE}. These observations confirm that the $[\bar{1}10]_O$-polarized $\boldsymbol{M}$ component is essential for activating IP-AHE.

Mirror-symmetry breaking in CRO/LCMO/CRO/NGO(110)$_O$ trilayers

The strong coupling between in-plane uniaxial MA and IP-AHE motivates us to evaluate the structural symmetries of CRO/LCMO/CRO/NGO(110)$_O$ trilayer heterostructures. The XRD RSMs near NGO(420)$_O$, (240)$_O$, (332)$_O$, and (33$\bar{2}$)$_O$ diffractions (Figs. 2a-d) confirm the orthorhombic symmetry of LCMO, CRO, and NGO unit-cells. According to detailed analyses of these RSM results (Supplementary Figs. 5, 6), these oxides have distinct orthorhombicity (defined as $d_{OR} = 1 - a_O/b_O$) but grow in a consistent axis-to-axis epitaxial relationship: CRO[100]$_O$//LCMO[100]$_O$//NGO[100]$_O$ and CRO[010]$_O$//LCMO[010]$_O$//NGO[010]$_O$[35,36]. For CRO and NGO, $d_{OR} > 0$, which is the direct consequence of the strong $a^-a^-c^+$-type OOR[35-37]. By contrast, LCMO shows $d_{OR} < 0$, which can be attributed to the Jahn-Teller distortion of the MnO_6 octahedra[38,39].

The heterointerfaces also play a key role in determining the structural symmetry of the LCMO layer in the heterostructure (Supplementary Figs. 7-9). The cross-sectional scanning transmission electron microscopy (STEM) images measured in high-angle annular dark-field (HAADF) mode confirm that both the top and bottom CRO/LCMO heterointerfaces are atomically-sharp (Supplementary Fig. 9). Although crystal symmetry of bulk LCMO is orthorhombic (space group: *Pbnm*), the top and bottom CRO/LCMO heterointerfaces will further eliminate specific mirror planes ($M_{(010)}$ and $M_{(100)}$) and rotation axes ($2_{[100]}$ and $2_{[010]}$), thus lowering the structural symmetry of the LCMO layer to monoclinic (space group: $P2_1/m$, see detailed analyses in Supplementary Fig. 7 and Supplementary Tables 1, 2).

The symmetry lowering in our CRO/LCMO/CRO trilayer can be visualized by converting the orthorhombic unit-cell into the pseudo-cubic unit-cell (denoted by the subscript "p", see Supplementary Fig. 8 for details). In these pseudo-cubic unit-cells, the c_p axis tilts towards the a_p axis while remaining perpendicular to the b_p axis ($\alpha = 90^o$ but $\beta \neq 90^o$), yielding a monoclinic-like distortion (as depicted in Fig. 2e). The layer-averaged tilting angle β can be directly calculated from the orthorhombicity d_{OR}[35,40,41]: for CRO and NGO with $d_{OR} > 0$, $\beta_{CR} < \beta_{NG} < 90°$, but for

LCMO with $d_{OR} < 0$, $\beta_{LC} > 90°$ (Fig. 2e). The opposite monoclinic-like tilting in the CRO and LCMO unit-cells is visible directly in an atomic-scale cross-sectional HAADF-STEM image (Fig. 2f). And the geometric phase analysis (GPA) on the large scale HAADF-STEM images (Figs. 2g,h and Supplementary Section 3) further confirm that the monoclinic-like tilting distortions in both CRO and LCMO layers are highly uniform. Additional high-resolution STEM images in annular bright-field (ABF) mode also reveal strong BO_6 octahedral coupling across the LCMO/CRO interfaces (Supplementary Fig. 11), which enables the axis-to-axis epitaxial relationship and thus the opposite monoclinic-like tilting distortions in CRO and LCMO. Moreover, the stronger OOR in CRO can propagate into LCMO by several u.c., enhancing the Jahn-Teller distortion and thus enlarging the d_{OR}[42-44]. Consequently, the LCMO layer in the trilayer heterostructure shows a stronger monoclinic-like distortion than both the bulk LCMO and the single-layer LCMO/NGO(110)$_O$ film (Supplementary Figs. 10, 12).

The RSM and STEM characterizations of the CRO/LCMO/CRO heterostructures suggest that the MnO_6 octahedral rotation/deformation and atomically-sharp interfaces cooperatively lower the structural symmetry of LCMO layers to monoclinic ($P2_1/m$). As depicted in Fig. 2i, in this monoclinic-distorted LCMO unit-cell, only one vertical mirror plane ($\perp[001]_O$) and a twofold rotation axis (along $[001]_O$) remain. Accordingly, the monoclinic tilting angle β_{LC} can be seen as a reliable parameter for evaluating the degree of mirror-symmetry breaking in the LCMO layer. Notably, the remaining symmetry operations define a C_{2h} point group, which allows $\boldsymbol{M}$ along the $[\bar{1}10]_O$ axis (the in-plane easy axis) to further break the remaining mirror-symmetry for activating IP-AHE[8,13].

Symmetry-engineered IP-AHE

Having established the microscopic structural symmetry of the CRO/LCMO/CRO trilayer heterostructures, we now turn to clarifying the origin of IP-AHE from the viewpoint of mirror-symmetry breaking. The relationship between intrinsic AHE current density $\boldsymbol{j}_{AHE}$, net Berry curvature ($\bar{\boldsymbol{\Omega}}$) vector, and the applied $\boldsymbol{E}$ is described by the following equation[2,3,8]:

$$\boldsymbol{j}_{AHE} = \frac{e^2}{\hbar}\bar{\boldsymbol{\Omega}} \times \boldsymbol{E} \qquad (1)$$

where the $\bar{\Omega} = \int [d\boldsymbol{k}]\, \Omega(\boldsymbol{k})\, f_0$, with $\Omega(\boldsymbol{k})$ the Berry curvature at crystal momentum $\boldsymbol{k}$ and f_0 the Fermi distribution function. In the conventional AHE case, $\bar{\boldsymbol{\Omega}}$ vector is parallel to the out-of-plane $\boldsymbol{M}$ vector, enforcing the orthogonal relationship $\boldsymbol{E} \perp \boldsymbol{M} \perp \boldsymbol{j}_{AHE}$. As mentioned above, the monoclinic-

distorted LCMO layer satisfies the mirror-symmetry breaking restriction for activating IP-AHE, which allows in-plane $\boldsymbol{M}//[\bar{1}10]_O$ to generate a non-zero $\bar{\boldsymbol{\Omega}}$ along film normal ($\bar{\Omega}_z$). The three vectors ($\boldsymbol{j}_{AHE}$, $\boldsymbol{E}$, and $\boldsymbol{M}$) then become coplanar, thus producing a pronounced IP-AHE[8, 10, 13]. Conversely, when $\boldsymbol{M}//[001]_O$, the $(001)_O$ mirror plane is preserved, thus suppressing $\bar{\Omega}_z$ and the IP-AHE (Fig. 1e).

To verify the key role of mirror-symmetry breaking-activated $\bar{\Omega}_z$ in inducing the IP-AHE, we track the evolution of ρ_{AHE} with the directions of $\boldsymbol{E}$ and $\boldsymbol{H}$. First, with fixed $\boldsymbol{E}//[\bar{1}10]_O$, we rotate the $\boldsymbol{H}$ vector in-plane (the angle between $\boldsymbol{H}$ and $[\bar{1}10]_O$ is defined as θ) and measure a series of the ρ_{AHE}-H curves (Supplementary Figs. 13, 14). The cosine-shaped ρ_{AHE}-θ curve (Supplementary Fig. 13) confirms the dominating role of in-plane $\boldsymbol{M}//[\bar{1}10]_O$ in inducing IP-AHE and thus reveals the dipolar structure of the $\bar{\boldsymbol{\Omega}}$ in spin-order space[13]. Second, we characterize the evolution of ρ_{AHE} by rotating $\boldsymbol{H}$ within the cross-sectional $(001)_O$ plane, and confirm that the IP-AHE is not induced by the out-of-plane component of misaligned in-plane $\boldsymbol{M}$ (Supplementary Figs. 15, 16). Third, with fixed $\boldsymbol{H}//[\bar{1}10]_O$, we rotate the $\boldsymbol{E}$ vector in-plane and found that the ρ_{AHE}-H hysteresis loops are independent of the E direction (Supplementary Fig. 17). This trend is in sharp contrast to the planar Hall effect but consistent with Eq. 1: a nonzero $\bar{\Omega}_z$-induced $\boldsymbol{j}_{AHE}$ should be insensitive to the in-plane orientation of $\boldsymbol{E}$.

Guided by the above results and analyses, we infer that IP-AHE in the CRO/LCMO/CRO trilayers could be effectively tuned by modulating the degree of mirror-symmetry breaking in LCMO layer. And the strongly coupled OOR patterns at the CRO/LCMO heterointerfaces could make t_{CRO} a potential tuning knob for this symmetry engineering. To verify this tuning scenario, we first calculate the in-plane anomalous Hall conductivity as $\sigma_{AHE} = \rho_{AHE}/(\rho_{xx})^2$ for parameterizing the IP-AHE, thereby eliminating the influence of t_{CRO}-dependent ρ_{xx}. Figs. 3a-e show the representative σ_{AHE}-H curves ($\boldsymbol{H}//[\bar{1}10]_O$) at 10 K, measured from a series of CRO/LCMO/CRO trilayer heterostructures with unequal t_{CRO}. The zero-field σ_{AHE} values display a non-monotonic t_{CRO}-dependence (Fig. 3f). As t_{CRO} increases, σ_{AHE} initially increases rapidly, peaks at t_{CRO} = 16 u.c., and then it decreases gradually. Owing to the strong uniaxial in-plane MA and associated square-like σ_{AHE}-H hysteresis loops, the optimal σ_{AHE} at zero-field is up to 103.7 mS·cm^{-1}, close to the saturated value (106.3 mS·cm^{-1}). Such a sizable zero-field IP-AHE was rarely observed in layered magnets with weak in-plane MA[14-18]. More strikingly, the $\beta_{LC} - 90°$ value (Fig. 3g), signifying the magnitude of monoclinic-like distortion in LCMO (Supplementary Figs. 3, 6, and

Supplementary Table 3), follows the same non-monotonic t_{CRO}-dependence as the σ_{AHE} (Fig. 3f). Because the NGO(110)$_O$ substrate has much weaker OOR than bulk CRO, the interfacial octahedral coupling at the CRO/NGO(110)$_O$ interface is expected to suppress the OOR in the ultrathin CRO buffer. Consequently, as t_{CRO} increases from 0 to 16 u.c., the OOR amplitude in CRO buffer rapidly approaches its bulk value, which increases the β_{LC} value, enlarges the mirror-symmetry breaking, and thus increases the σ_{AHE}. Nevertheless, further increasing t_{CRO} could lead to considerable strain-relaxation and formation of *a/b* twin domains, thus reducing the β_{LC} and σ_{AHE}.

The IP-AHE of CRO/LCMO/CRO trilayer also shows strong *T*-dependence. As shown in Supplementary Fig. 18, nonzero σ_{AHE} persists up to 200 K. Upon cooling, all of the σ_{AHE}-*T* curves exhibit a clear σ_{AHE} increment at $T < 80$ K, consistent with the reduction of ρ_{xx}. For the trilayer samples with relatively weak IP-AHE ($t_{CRO} \geq 32$ u.c. or $t_{CRO} \leq 8$ u.c.), σ_{AHE} reverses sign from negative to positive near 100 K upon warming. Such a sign-reversal behavior is similar to the intrinsic AHE of SRO thin films, which is sensitive to the band topology[4, 23].

Based on the above experimental results, we perform first-principles density-functional-theory (DFT) calculations to further elucidate the link between $\bar{\Omega}_z$, structural symmetry, and IP-AHE in LCMO. Considering that the β_{LC} serves as a reliable control parameter of the mirror-symmetry breaking and thus the IP-AHE, we construct four different (110)$_O$-oriented LCMO 2×2×2 supercells: one cubic supercell without any OOR and three orthorhombic supercells with $a^-a^-c^+$-type OOR and Jahn-Teller distortion. The variable amplitudes of OOR and Jahn-Teller distortions in the orthorhombic supercells give rise to unequal $\beta_{LC} = 90.0°$, 90.08°, and 90.16° (Supplementary Fig. 19). The Wannier bands show excellent agreement with the DFT results (Supplementary Fig. 20), validating the following AHE and Berry curvature calculations. After imposing ***M*** along the $[\bar{1}10]_O$ axis, DFT-calculated σ_{AHE} (σ_{DFT}) vanishes in the cubic supercell but remains finite in all the orthorhombic supercells, even for the one with $\beta_{LC} = 90.0°$ (Figs. 3h, i and Supplementary Fig. 21). The magnitude of σ_{DFT} increases monotonically with β_{LC}, consistent with the experimental trend. The stark contrasts of σ_{DFT} between the cubic and orthorhombic supercells strongly suggest that the MnO_6 octahedral rotation/deformation and the associated mirror-symmetry breaking dominate the emergence and tunability of IP-AHE. In the practical CRO/LCMO/CRO/NGO(110)$_O$ trilayer heterostructures, the OOR and Jahn-Teller distortion in LCMO are strongly coupled with the monoclinic-like tilt, making β_{LC} the experimental tuning knob of IP-AHE. Following the ***H***-

direction-dependent IP-AHE shown in Supplementary Fig. 13, we also calculate the evolution of non-zero σ_{DFT} with the orientation of in-plane $\boldsymbol{M}$ vector (Supplementary Fig. 22). These results again confirm the critical role of the uniaxial $\boldsymbol{M}//[\bar{1}10]_O$ in activating $\bar{\Omega}_z$ and inducing IP-AHE.

Electrical control of IP-AHE via ionic-liquid gating

After establishing the OOR-mediated symmetry-engineering of $\bar{\Omega}_z$ in the CRO/LCMO/CRO trilayers, we employ an ionic liquid gating (ILG) approach (see Methods for procedural details) to achieve in situ electrical modulation of IP-AHE. As schematically illustrated in Figs. 4a,b, a positive gate voltage (V_g) electrolyzes residual water in the ionic liquid and then triggers proton intercalation into the CRO/LCMO/CRO trilayers[45]. Previous reports have revealed that such a protonation process can induce both electron doping and structural transformations in perovskite oxide heterostructures[45, 46]. Accordingly, ILG is expected to effectively tune the symmetry-coupled IP-AHE. As shown in Figs. 4c,d, increasing V_g from 0 to 1.0 V leads to negligible changes in the σ_{AHE}-H curves. When V_g exceeds 1.1 V, σ_{AHE} starts to decrease progressively and vanishes at V_g = 1.4 V. In contrast to this effective suppression of IP-AHE, the H_C values remain nearly unchanged during protonation, suggesting a nearly invariant macroscopic ferromagnetism in LCMO layer. According to previous literature, ILG-driven protonation in ruthenates occurs at a relatively low threshold $V_g \leq 1.5$ V and completes within a narrow V_g range (~0.5 V)[47,48]. In contrast, the protonation in manganites typically occurs at a much higher threshold $V_g > 2.5$ V, and continuously evolves over a wider V_g range (>1.0 V)[49]. Therefore, during the ILG of our CRO/LCMO/CRO trilayer, the sharp changes in σ_{AHE} at 1.1 V $\leq V_g \leq$1.4 V should coincide with the protonation occurring first in the CRO layers, forming an H_xCaRuO_3 phase[48]. Furthermore, by alternatively applying positive (+1.4 V) and negative (−1.0 V) V_g to drive structural transformations between CRO and H_xCaRuO_3, we can reversibly switch the IP-AHE ON and OFF (Supplementary Fig. 23).

Consistent with the evolutions of IP-AHE during ILG, the XRD 2θ-ω linear scans measured in the small V_g range (0~1.5 V) display a clear CRO(440)$_O$ peak shift towards lower Bragg angles, while the LCMO(440)$_O$ peak position remains nearly unchanged (Supplementary Fig. 24). DFT calculations further indicate that the protonation in CRO effectively reduces the OOR in H_xCaRuO_3[48], especially the out-of-plane tilting (Fig. 4b and Supplementary Figs. 25, 26), thereby lowering the OOR in the adjacent LCMO layer through interfacial octahedral coupling (Supplementary Fig. 27). Consequently, the CRO/LCMO/CRO trilayer exhibits effective and reversible suppressions of IP-AHE with minimal change in ferromagnetism.

Conclusion

we established a ferromagnetic CRO/LCMO/CRO/NGO(110)$_O$ heterostructure as a symmetry-engineered and electrically tunable platform for IP-AHE. In this trilayer epitaxial system, the corner-sharing octahedral framework and atomically sharp CRO/LCMO heterointerfaces, together with the uniaxially-aligned in-plane $\boldsymbol{M}$, cooperatively break the vertical mirror-symmetries in the LCMO layer and activate non-zero $\overline{\Omega}_z$. The resulting IP-AHE faithfully tracks the square-shaped ferromagnetic hysteresis loops, and persists at zero field up to 200 K. By adjusting the t_{CRO}, we deliberately reconfigure the degree of mirror-symmetry breaking and establish its intimate correlation with σ_{AHE}. By introducing protonation via ILG, we further realize a wide-range electrical modulation and reversible ON/OFF switching of IP-AHE.

This symmetry engineering strategy for IP-AHE should be broadly applicable across magnetic heterostructures and layered magnets with rich lattice degrees of freedom. Fundamentally, the symmetry-tailored IP-AHE offers a powerful fingerprint for uncovering intimate links between quantum geometry and nontrivial magnetic orders/spin textures. Practically, the electrically tunable IP-AHE enables planar-geometry-compatible Hall readout of spin transport and magnetic switching, opening an avenue toward programmable Hall functionalities and innovative spintronic and magnetoelectric device architectures.

References

1. Xiao, D., Chang, M.-C. & Niu, Q. Berry phase effects on electronic properties. *Reviews of Modern Physics* **82**, 1959-2007 (2010).
2. Nagaosa, N., Sinova, J., Onoda, S., MacDonald, A. H. & Ong, N. P. Anomalous Hall effect. *Reviews of Modern Physics* **82**, 1539-1592 (2010).
3. Fert, A., Ramesh, R., Garcia, V., Casanova, F.,& Bibes, M. Electrical control of magnetism by electric field and current-induced torques. *Reviews of Modern Physics* **96,** 015005 (2024).
4. Fang, Z. *et al.* The Anomalous Hall Effect and Magnetic Monopoles in Momentum Space. *Science* **302**, 92-95 (2003).
5. Hua, E. *et al.* Ru-Doping-Induced Spin Frustration and Enhancement of the Room-Temperature Anomalous Hall Effect in $La_{2/3}Sr_{1/3}MnO_3$ Films. *Advanced Materials* **34**, 2206685 (2022).
6. Deng, Y. *et al.* Gate-tunable room-temperature ferromagnetism in two-dimensional Fe_3GeTe_2. *Nature* **563**, 94-99 (2018).
7. Landau, L. D. *et al. Electrodynamics of continuous media*. Vol. 8 (elsevier, 2013).
8. Tan, H., Liu, Y. & Yan, B. Unconventional anomalous Hall effect from magnetization parallel to the electric field. *Physical Review B* **103**, 214438 (2021).
9. Liu, X., Hsu, H.-C. & Liu, C.-X. In-Plane Magnetization-Induced Quantum Anomalous Hall Effect. *Physical Review Letters* **111**, 086802 (2013).
10. Liu, Z. *et al.* Intrinsic Quantum Anomalous Hall Effect with In-Plane Magnetization: Searching Rule and Material Prediction. *Physical Review Letters* **121**, 246401 (2018).
11. Cao, J. *et al.* In-Plane Anomalous Hall Effect in PT-Symmetric Antiferromagnetic Materials. *Physical Review Letters* **130**, 166702 (2023).
12. Kurumaji, T. Symmetry-based requirement for the measurement of electrical and thermal Hall conductivity under an in-plane magnetic field. *Physical Review Research* **5**, 023138 (2023).
13. Liu, Z., Wei, M., Hou, D., Gao, Y. & Niu, Q. Multipolar anisotropy in anomalous Hall effect from spin-group symmetry breaking. *Physical Review X* **15**, 031006 (2025).
14. Zhou, J. *et al.* Heterodimensional superlattice with in-plane anomalous Hall effect. *Nature* **609**, 46-51 (2022).
15. Ge, J. *et al.* Unconventional Hall effect induced by Berry curvature. *National Science Review* **7**, 1879-1885 (2020).
16. Wang, L. *et al.* Orbital Magneto-Nonlinear Anomalous Hall Effect in Kagome Magnet Fe_3Sn_2. *Physical Review Letters* **132**, 106601 (2024).
17. Wang, L. *et al.* In-plane Hall effect in $Co_3Sn_2S_2$. *Physical Review B* **111**, 054412 (2025).
18. Nakamura, A. *et al.* In-Plane Anomalous Hall Effect Associated with Orbital Magnetization: Measurements of Low-Carrier Density Films of a Magnetic Weyl Semimetal. *Physical Review Letters* **133**, 236602 (2024).
19. Rondinelli, J. M., May, S. J. & Freeland, J. W. Control of octahedral connectivity in perovskite oxide heterostructures: An emerging route to multifunctional materials discovery. *MRS Bulletin* **37**, 261-270 (2012).
20. Rondinelli, J. M. & Spaldin, N. A. Structure and Properties of Functional Oxide Thin Films: Insights From Electronic-Structure Calculations. *Advanced Materials* **23**, 3363-3381 (2011).
21. Howard, C. J. & Stokes, H. T. Group-theoretical analysis of octahedral tilting in perovskites. *Structural*

Science **54**, 782-789 (1998).

22. Glazer, A. M. The classification of tilted octahedra in perovskites. *Acta Crystallographica Section B: Structural Crystallography and Crystal Chemistry* **28**, 3384-3392 (1972).
23. Tian, D. *et al.* Manipulating Berry curvature of $SrRuO_3$ thin films via epitaxial strain. *Proceedings of the National Academy of Sciences* **118**, e2101946118 (2021).
24. Mathieu, R. *et al.* Scaling of the Anomalous Hall Effect in $Sr_{1-x}Ca_xRuO_3$. *Physical review letters* **93**, 016602 (2004).
25. Hellman, F. *et al.* Interface-induced phenomena in magnetism. *Reviews of Modern Physics* **89**, 025006 (2017).
26. Wang, L. *et al.* Ferroelectrically tunable magnetic skyrmions in ultrathin oxide heterostructures. *Nature Materials* **17**, 1087-1094 (2018).
27. Hong, S. S. *et al.* Extreme tensile strain states in $La_{0.7}Ca_{0.3}MnO_3$ membranes. *Science* **368**, 71-76 (2020).
28. Zhang, J. *et al.* A correlated ferromagnetic polar metal by design. *Nature Materials* **23**, 912-919 (2024).
29. Liu, L. *et al.* Symmetry-dependent field-free switching of perpendicular magnetization. *Nature Nanotechnology* **16**, 277-282 (2021).
30. Chen, B. B. *et al.* Contrasting size-scaling behavior of ferromagnetism in $La_{0.67}Ca_{0.33}MnO_3$ films and $La_{0.67}Ca_{0.33}MnO_3/CaRuO_3$ multilayers. *Applied Physics Letters* **104** 242416 (2014).
31. Zhong, Z. & Hansmann, P. Band Alignment and Charge Transfer in Complex Oxide Interfaces. *Physical Review X* **7**, 011023 (2017).
32. Chen, P. F. *et al.* High-T_C ferromagnetic order in $CaRuO_3/La_{2/3}Ca_{1/3}MnO_3$ superlattices. *Applied Physics Letters* **103** 262402 (2013).
33. Boschker, H. *et al.* Strong uniaxial in-plane magnetic anisotropy of (001)-and (011)-oriented $La_{0.67}Sr_{0.33}MnO_3$ thin films on $NdGaO_3$ substrates. *Physical Review B* **79**, 214425 (2009).
34. Chen, B. B. *et al.* All-oxide–based synthetic antiferromagnets exhibiting layer-resolved magnetization reversal. *Science* 357, 191-194 (2017).
35. Huang, Z. *et al.* Tuning the ground state of $La_{0.67}Ca_{0.33}MnO_3$ films via coherent growth on orthorhombic $NdGaO_3$ substrates with different orientations. *Physical Review B* **86**, 014410 (2012).
36. Zayak, A. T., Huang, X., Neaton, J. B. & Rabe, K. M. Structural, electronic, and magnetic properties of $SrRuO_3$ under epitaxial strain. *Physical Review B* **74**, 094104 (2006).
37. Chang, S. H. *et al.* Thickness-dependent structural phase transition of strained $SrRuO_3$ ultrathin films: The role of octahedral tilt. *Physical Review B* **84**, 104101 (2011).
38. Wang, L. F. *et al.* Annealing assisted substrate coherency and high-temperature antiferromagnetic insulating transition in epitaxial $La_{0.67}Ca_{0.33}MnO_3/NdGaO_3(001)$ films. *AIP Advances* **3** (2013).
39. Tokura, Y. Critical features of colossal magnetoresistive manganites. *Reports on Progress in Physics* **69**, 797 (2006).
40. Gao, G., Yin, Z., Huang, Z., Jin, S. & Wu, W. The thickness evolution of orthorhombic lattice distortions in heteroepitaxial $La_{0.67}Ca_{0.33}MnO_3/NdGaO_3(110)_{Or}$ observed by x-ray reciprocal space mapping. *Journal of Physics D: Applied Physics* **41**, 152001 (2008).
41. Aso, R., Kan, D., Shimakawa, Y. & Kurata, H. Atomic level observation of octahedral distortions at the perovskite oxide heterointerface. *Scientific reports* **3**, 2214 (2013).
42. He, J., Borisevich, A., Kalinin, S. V., Pennycook, S. J. & Pantelides, S. T. Control of Octahedral Tilts and Magnetic Properties of Perovskite Oxide Heterostructures by Substrate Symmetry. *Physical Review*

Letters **105**, 227203 (2010).

43. Borisevich, A. Y. *et al.* Suppression of Octahedral Tilts and Associated Changes in Electronic Properties at Epitaxial Oxide Heterostructure Interfaces. *Physical Review Letters* **105**, 087204 (2010).
44. Kan, D. *et al.* Tuning magnetic anisotropy by interfacially engineering the oxygen coordination environment in a transition metal oxide. *Nature Materials* **15**, 432-437 (2016).
45. Lu, N. *et al.* Electric-field control of tri-state phase transformation with a selective dual-ion switch. *Nature* **546**, 124-128 (2017).
46. Guan, Y., Han, H., Li, F., Li, G. & Parkin, S. S. P. Ionic Gating for Tuning Electronic and Magnetic Properties. *Annual Review of Materials Research* **53**, 25-51 (2023).
47. Li, Z. *et al.* Reversible manipulation of the magnetic state in $SrRuO_3$ through electric-field controlled proton evolution. *Nature Communications* **11**, 184 (2020).
48. Shen, S. *et al.* Emergent Ferromagnetism with Fermi-Liquid Behavior in Proton Intercalated $CaRuO_3$. *Physical Review X* **11**, 021018 (2021).
49. Cui, B. *et al.* Reversible Ferromagnetic Phase Transition in Electrode-Gated Manganites. *Advanced Functional Materials* **24**, 7233-7240 (2014).

Methods

Thin film growth

We grow epitaxial $CaRuO_3(t_{CRO})/La_{2/3}Ca_{1/3}MnO_3$(32 u.c.)/$CaRuO_3(t_{CRO})$ (CRO/LCMO/CRO) trilayer heterostructures on $NdGaO_3(110)_O$ [$NGO(110)_O$] substrates by pulsed laser deposition (KrF excimer laser, λ = 248 nm). Before growth, we anneal the $NGO(110)_O$ substrates at 1000 °C for 4 h to obtain single-unit-cell-height surface terraces. During the growth of CRO and LCMO layers, we set the substrate temperature to 700 °C and the laser fluence to 1.8 J cm^{-2}. We set the oxygen partial pressure (P_{O2}) to 7.5 Pa for CRO and 30 Pa for LCMO. We monitor and optimize the growth rate and mode using reflection high-energy electron diffraction (RHEED). After deposition, we anneal the heterostructures in situ for 15 min under the growth conditions and then cool them down to room temperature in an oxygen atmosphere of P_{O2} = 2000 Pa.

Structural, Magnetic, and Electrical Characterizations

We perform the structural characterizations of the trilayer heterostructures using a high-resolution X-ray diffractometer (PANalytical Empyrean, Cu Kα_1 radiation) in 2θ–ω scan and reciprocal-space-mapping (RSM) modes. We prepare cross-sectional scanning transmission electron microscopy (STEM) specimens by focused ion beam (Ga^+) milling to a thickness of ~30 nm. We perform cross-sectional STEM on a Thermo Scientific Themis Z microscope operated at 300 keV and equipped with a spherical aberration corrector for the condenser lens. We acquire atomic-resolution STEM images using a 25 mrad convergent semi-angle, with collection angles of 41-200 mrad for high-angle annular dark-field (HAADF) and 13-25 mrad for annular bright-field (ABF) imaging. We measure the magnetic properties of the trilayer heterostructures using a vibrating sample magnetometer (VSM-SQUID). We measure temperature- and field-dependent ρ_{xx} and ρ_{xy} using a custom-built physical property measurement system equipped with a rotational sample stage and a 7 T superconducting magnet. To perform the Hall measurements, we pattern the heterostructures into six-probe Hall bars using photolithography.

Density-Functional Theory Calculations

We perform density-functional theory (DFT) calculations to investigate the structural, electronic, and magnetic properties of $La_{2/3}Ca_{1/3}MnO_3$ using the Vienna *ab initio* Simulation Package (VASP)[50, 51], with the Perdew–Burke–Ernzerhof (PBE) generalized gradient approximation (GGA)[52] for exchange–correlation. To model Ca substitution in $LaMnO_3$, we employ the virtual crystal approximation (VCA)[53]. We construct a 2×2×2 supercell (based on the pseudo-cubic unit-cell of $La_{2/3}Ca_{1/3}MnO_3$) by reorienting the tetragonal unit-cell so that the new *c*-axis aligns with the $[110]_O$ direction of the original lattice, which yields a $\sqrt{2} \times \sqrt{2} \times 1$ expansion of the original tetragonal cell.

We use a plane-wave cutoff energy of 550 eV and fully relax the structure until the residual forces on all atoms are below 0.01 eV/Å. After structural optimization, we calculate the electronic band structure using the WIEN2k package[54,55] with a 7×7×7 Monkhorst–Pack k-point mesh. To account for strong correlation effects and spin–orbit coupling (SOC) in the Mn 3d orbitals, we perform DFT + U + SOC calculations with U = 8.0 eV and J = 2.0 eV[56]. We project the Mn 3d states onto maximally localized Wannier functions (MLWFs)[57] using Wannier90 code[58] through the Wien2Wannier interface[59]. We then use the resulting tight-binding Hamiltonian to compute the intrinsic anomalous Hall conductivity (AHC) with Wannier90[58] by integrating the Berry curvature over the occupied states across the Brillouin zone.

Ionic Liquid Gating (ILG)

Before the in situ XRD and magnetotransport measurements of ILG-induced structural changes, we deposit Pt electrodes along the film edges by DC ion sputtering as bottom contacts, and then we use a thin Pt plate as the top electrode. We then place a droplet of commercial ionic liquid (DEME–TFSI^{+-}) to cover both the film surface and the Pt plate. We apply the bias using a Keithley 2450: we hold the potential between the bottom and top electrodes at 0 V and then ramp it to the target value while continuously recording XRD spectra and Hall signals.

Data availability

All data relevant to the conclusions of this study are available from

Reference

50. Kresse, G. & Hafner, J. Ab initio molecular-dynamics simulation of the liquid-metal--amorphous-semiconductor transition in germanium. Physical Review B 49, 14251-14269 (1994).
51. Kresse, G. & Furthmüller, J. Efficient iterative schemes for ab initio total-energy calculations using a plane-wave basis set. *Physical Review B* **54**, 11169-11186 (1996).
52. Perdew, J. P., Burke, K. & Ernzerhof, M. Generalized Gradient Approximation Made Simple. *Physical Review Letters* **77**, 3865-3868 (1996).
53. Bellaiche, L. & Vanderbilt, D. Virtual crystal approximation revisited: Application to dielectric and piezoelectric properties of perovskites. *Physical Review B* **61**, 7877-7882 (2000).
54. Schwarz, K., Blaha, P. & Madsen, G. K. H. Electronic structure calculations of solids using the WIEN2k package for material sciences. *Computer Physics Communications* **147**, 71-76 (2002).
55. Blaha, P., Schwarz, K., Madsen, G., Kvasnicka, D. & Luitz, J. WIEN2k: An Augmented Plane Wave plus Local Orbitals Program for Calculating Crystal Properties. *Technische Universität Wien, Wien* **28** (2001).
56. Mellan, T. A., Corà, F., Grau-Crespo, R. & Ismail-Beigi, S. Importance of anisotropic Coulomb interaction in $LaMnO_3$. *Physical Review B* **92**, 085151 (2015).
57. Marzari, N., Mostofi, A. A., Yates, J. R., Souza, I. & Vanderbilt, D. Maximally localized Wannier functions: Theory and applications. *Reviews of Modern Physics* **84**, 1419-1475 (2012).
58. Mostofi, A. A. *et al.* wannier90: A tool for obtaining maximally-localised Wannier functions. *Computer*

Physics Communications **178**, 685-699 (2008).

59. Kuneš, J. *et al.* Wien2wannier: From linearized augmented plane waves to maximally localized Wannier functions. *Computer Physics Communications* **181**, 1888-1895 (2010).

Acknowledgments

This work is supported by the National Key Research and Development Program of China (Grant No. 2023YFA1406404), the National Natural Science Foundation of China (Grant Nos. 52521006, 52572144, 12504152, 12374094, 12304153, 12422407, and 12304035), Quantum Science and Technology-National Science and Technology Major Project (Grant No. 2024ZD0301300), CAS Project for Young Scientists in Basic Research (No. YSBR-084), Anhui Provincial Natural Science Foundation (Grant No. 2308085MA15). The computational resource is provided by the National Supercomputing Center (Xi'an) in Northwest University. Synchrotron X-ray diffraction characterizations were supported by BL02U2 at the Shanghai Synchrotron Radiation Facility. The device fabrication was partially carried out at the Center for Micro and Nanoscale Research and Fabrication, University of Science and Technology of China. And the electrical characterizations were carried out at Instruments Center for Physical Science, University of Science and Technology of China.

Author contributions

L.W. and W.W. conceived the idea and supervised the project. K.D. completed the theoretical analysis of the symmetry of IP-AHE under the guidance of L.W., W.W. and Y.G.. K.D., Z.W., and Wf.W. contributed equally to this work. K.D. prepared the samples with the help of F.J., E.H., J.L., J.Z, Y.Z. K.D. performed the magnetotransport and electrical transport characterizations with the help of K.L., H.Y., Q.L., Z.L., A.W. K.D. regulated the sample with ILG with the help of S.S. and L.Y. Z.W. supervised the STEM measurements and analyzed the data. Wf.W. and N. L. provided the DFT calculations under the guidance of L.S., L.W., W.W. and K.D. wrote the manuscript, with contributions from all authors.

Competing interests

The authors declare no competing interests.

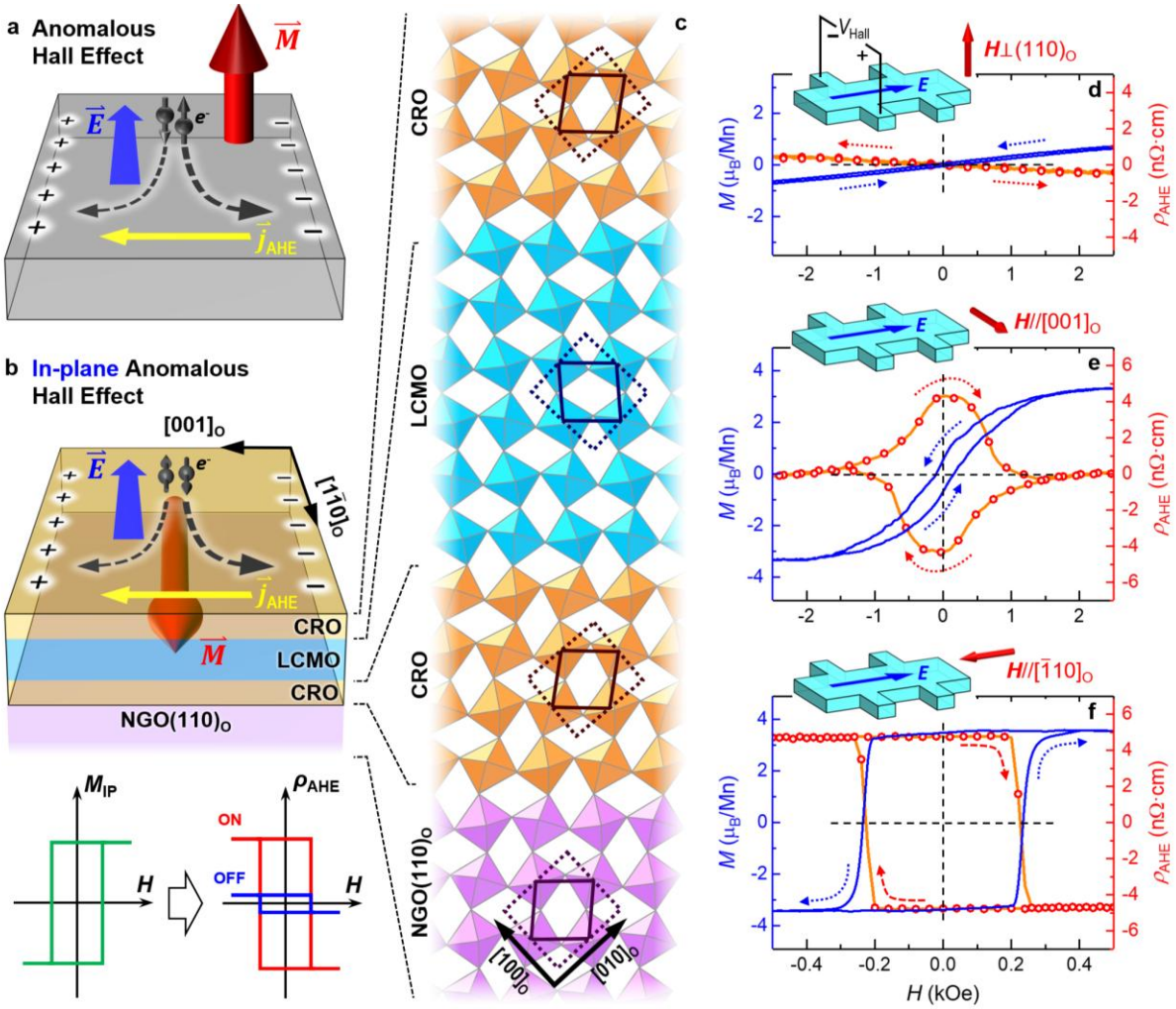


Fig. 1| Observation of in-plane anomalous Hall effect in $CaRuO_3/La_{2/3}Ca_{1/3}MnO_3/CaRuO_3$ trilayer. (**a**) Schematic illustration of conventional anomalous Hall effect (AHE), where the three vectors, magnetization (***M***), longitudinal electric field (***E***), and transverse Hall current density ($\boldsymbol{j}_{AHE}$), are mutually orthogonal. (**b**) Upper panel: Schematic stacking sequence of $CaRuO_3/La_{2/3}Ca_{1/3}MnO_3/CaRuO_3$ (CRO/LCMO/CRO) trilayer heterostructure grown on $NdGaO_3(110)_O$ [$NGO(110)_O$] substrate and schematic illustration of in-plane anomalous Hall effect (IP-AHE), where the in-plane ***M*** and ***E*** vector also can generate $\boldsymbol{j}_{AHE}$. Lower panel: schematic line shapes of magnetic field (H) dependent in-plane M (M_{IP}) and anomalous Hall resistivity (ρ_{AHE}) of a tunable IP-AHE system, where the magnitude of ρ_{AHE}-H hysteresis can be turned ON and OFF. (**c**) Schematic illustration of corner-shared BO_6 oxygen octahedral rotation/deformation patterns in a CRO/LCMO/CRO/$NGO(110)_O$ trilayer heterostructure. The A-site cations are hidden for clarity. The orthorhombic and pseudo-cubic unit-cells are labeled by dashed and solid boxes, respectively. (**d-f**) M-H and ρ_{AHE}-H curves measured from a CRO(16 u.c.)/LCMO(32 u.c.)/CRO(16 u.c.)/$NGO(110)_O$ heterostructure at 10 K, with ***H***⊥$(110)_O$ plane (d), ***H***//$[001]_O$ (e), and ***H***//$[\bar{1}10]_O$ (f). ***E*** is fixed along the $[\bar{1}10]_O$ axis for all the AHE and IP-AHE measurements. The Hall voltage (V_{Hall}) corresponding to positive ρ_{AHE} are also marked in the inset of (d).

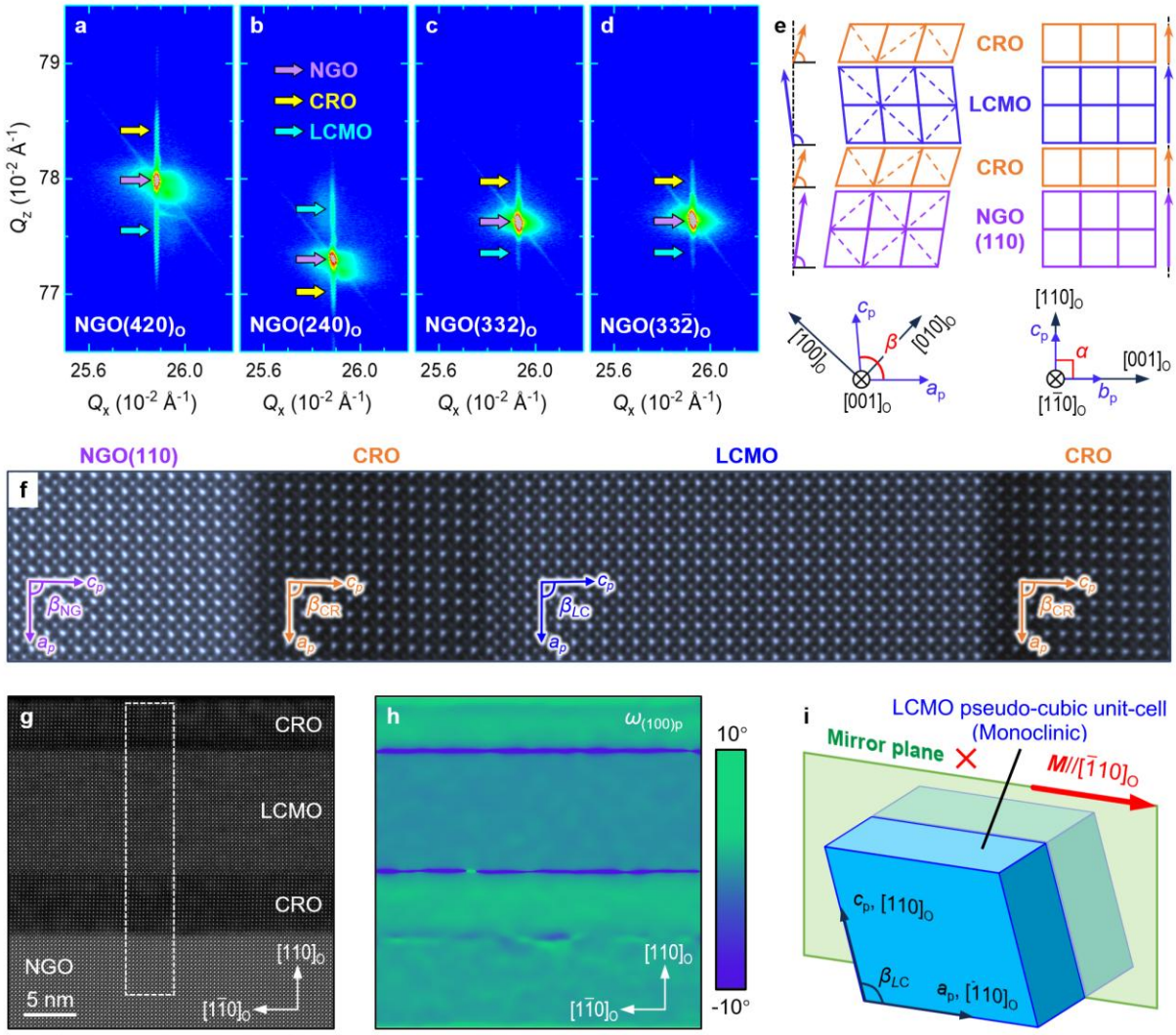


Fig. 2| Structural characterizations on the CRO/LCMO/CRO trilayer heterostructure. (**a-d**) Reciprocal space mappings measured from the CRO(16 u.c.)/LCMO(32 u.c.)/CRO(16 u.c.)/NGO(110)$_O$ sample near the NGO(420), (240), (332), and (33$\bar{2}$) diffractions. The diffractions from CRO, LCMO, and NGO are marked by solid arrows in orange, blue, and purple, respectively. (**e**) Schematics of the monoclinic-like tilting of pseudo-cubic CRO, LCMO, and NGO unit-cells, viewed along $[001]_O$ and $[\bar{1}10]_O$ axes. The angle between $(110)_O$ and $(1\bar{1}0)_O$ planes is labeled as β. Variations of β in CRO, LCMO, and NGO are marked by solid arrows. The angle between $(110)_O$ and $(001)_O$ planes is labeled as α. For all of the oxide layers, $\alpha = 90°$. (**f**) Zoom-in HAADF-STEM image of the CRO(16 u.c.)/LCMO(32 u.c.)/CRO(16 u.c.)/NGO(110)$_O$ sample, viewed along the $[001]_O$ zone axis. This high-resolution image can clearly resolve the β angles of LCMO, CRO, and NGO. (**g**) Large-scale HAADF-STEM images viewed along the $[001]_O$ zone axis. The region for acquiring the zoom-in HAADF-STEM image shown in (f) is marked by a white box. (**h**) Geometric phase analysis [based on the HAADF-STEM image (g)] of the $(\bar{1}10)_O$ $[(100)_p]$ plane tilting angle [defined as $\omega_{(100)p}$]. (**i**) Schematic pseudo-cubic LCMO unit-cell with monoclinic-like distortion. The light green rectangle indicates the only one mirror plane left in LCMO, which can be broken by the ***M*** vector parallel to $[\bar{1}10]_O$ axis.

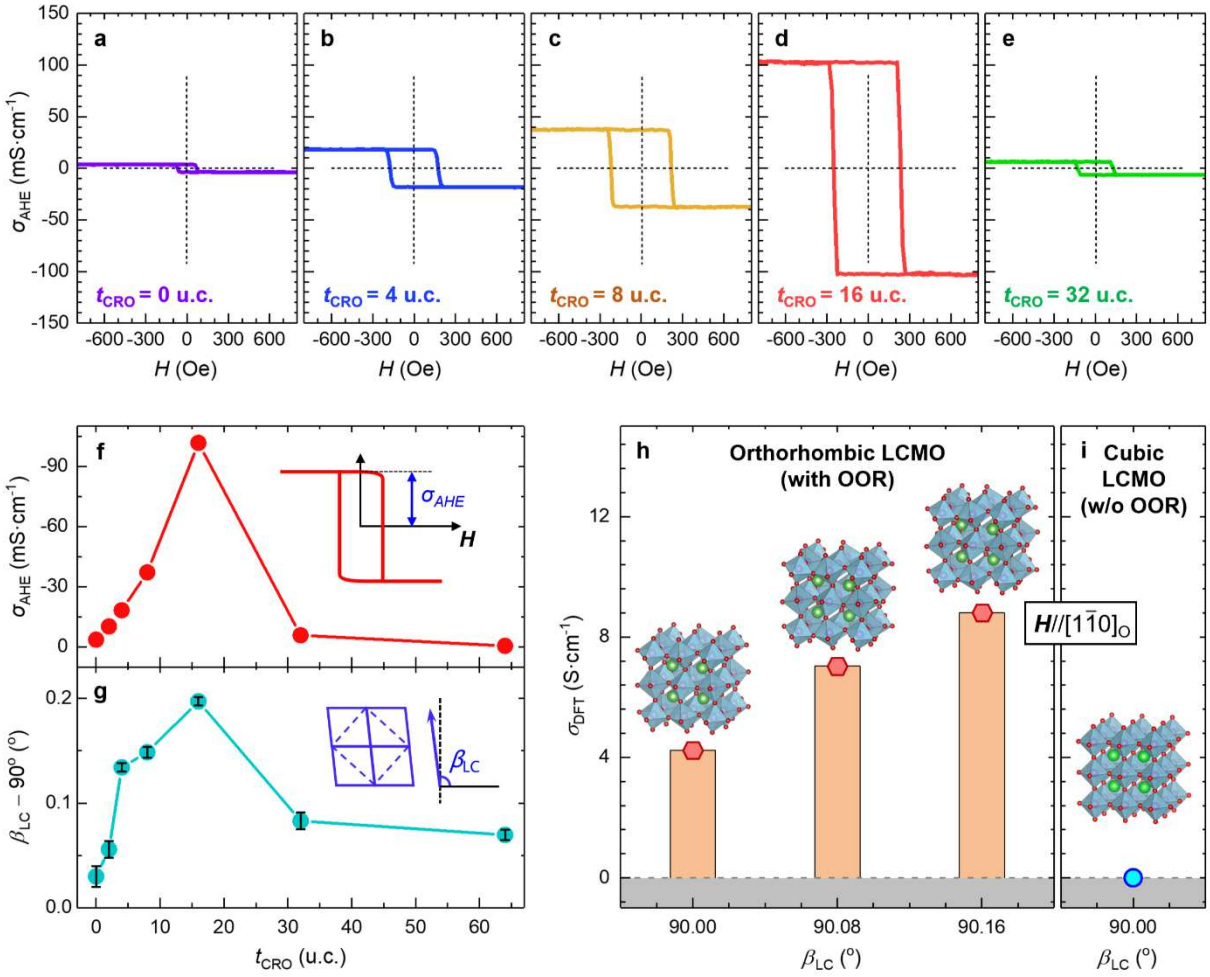


Fig. 3| Symmetry-tailored IP-AHE of CRO/LCMO/CRO trilayer heterostructures.
(**a-e**) *H*-dependent anomalous Hall conductivity (σ_{AHE}-*H*) curves measured from a series of CRO/LCMO/CRO/NGO(110)$_O$ heterostructures with various CRO layer thicknesses (t_{CRO}). All the measurements are conducted at 10 K with ***E***//***H***//LCMO[$\bar{1}$10]$_O$. (**f,g**) t_{CRO}-dependent zero-field σ_{AHE} (f) and β_{LC}−90˚ (g) values at 10 K. The schematic insets illustrate the definitions of these two parameters. (**h,i**) DFT-calculated σ_{AHE} (σ_{DFT}) of orthorhombic LCMO supercells with various β_{LC} values and cubic LCMO supercell (β_{LC} = 90˚) without any OOR.

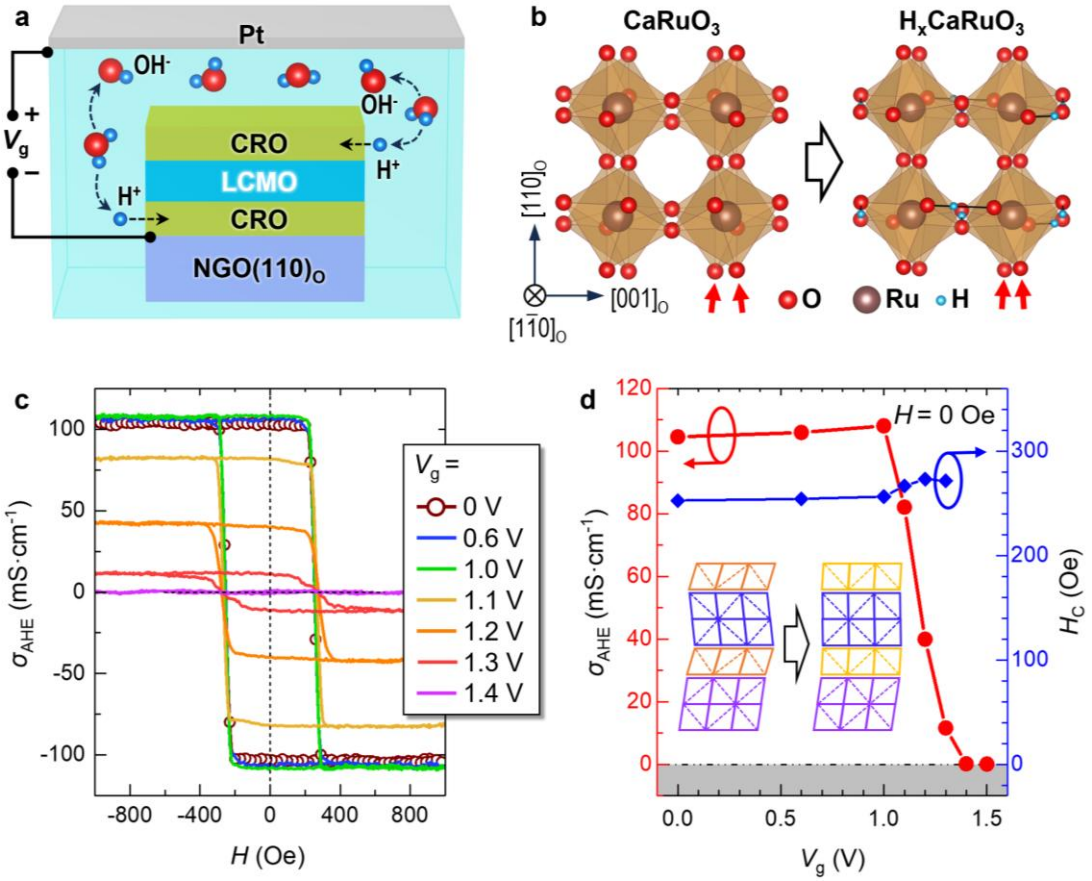


Fig. 4| Ionic liquid gating of IP-AHE in the CRO/LCMO/CRO trilayer heterostructure.
(**a**) Schematic illustration of the protonation of CRO/LCMO/CRO trilayer through ionic liquid gating. The gating voltage (V_g) is applied between the Pt top electrode and the conductive trilayer sample. (**b**) DFT-optimized structure of pristine $CaRuO_3$ and proton-intercalated H_xCaRuO_3 (x = 1) unit-cells viewed along $[\bar{1}10]_O$ axis. The protonation-induced reduction of octahedral tilting is marked by solid (red) arrows. The A-site Ca cations are hidden for clarity. (**c**) σ_{AHE}-H curves measured from a CRO(16 u.c.)/LCMO(32 u.c.)/CRO(16 u.c.)/$NGO(110)_O$ heterostructure with various V_g. All the Hall measurements are conducted at 10 K with ***E***//***H***//LCMO$[\bar{1}10]_O$. (**d**) V_g-dependent σ_{AHE} at zero field and the H_C values extracted from the σ_{AHE}-H curves. The insets illustrate the reduction of monoclinic-like distortions in CRO and LCMO unit-cells after protonation.

Supplementary Files

This is a list of supplementary files associated with this preprint. Click to download.

- IPAHEsupplementarymaterials.pdf